IEEE Photonics Journal
An IEEE Photonics Society Publication

Open Access

Phase Interrogation of Diaphragm-Based Optical Fiber Acoustic Sensor Assisted by Wavelength-Scanned Spectral Coding

Volume 10, Number 3, June 2018

Xin Fu
Ping Lu
Wenjun Ni
Hao Liao
Xinyue Jiang
Deming Liu
Jiangshan Zhang

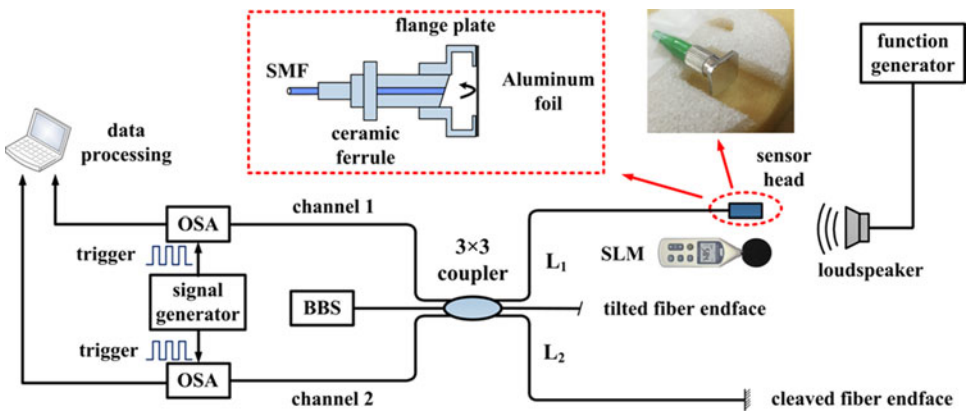

DOI: 10.1109/JPHOT.2018.2827059
1943-0655 © 2018 IEEE

IEEE photonics SOCIETY

IEEE

Phase Interrogation of Diaphragm-Based Optical Fiber Acoustic Sensor Assisted by Wavelength-Scanned Spectral Coding

Xin Fu,[1] Ping Lu,[1] Wenjun Ni,[1] Hao Liao,[1] Xinyue Jiang,[1] Deming Liu,[1] and Jiangshan Zhang[2]

[1]National Engineering Laboratory for Next Generation Internet Access System, School of Optical and Electronic Information, Huazhong University of Science and Technology, Wuhan 430074, China
[2]Department of Electronics and Information Engineering, Huazhong University of Science and Technology, Wuhan 430074, China

DOI:10.1109/JPHOT.2018.2827059

Manuscript received March 15, 2018; revised April 10, 2018; accepted April 11, 2018. Date of publication April 16, 2018; date of current version May 11, 2018. This work was supported in part by the National Natural Science Foundation of China under Grants 61775070 and 61275083, and in part by the Fundamental Research Funds for the Central Universities under Grant 2017KFYXJJ032. Corresponding author: Ping Lu (e-mail: pluriver@mail.hust.edu.cn).

Abstract: In this paper, we proposed a phase interrogation method for diaphragm-based interferometric optical fiber acoustic sensor based on the spectral coding process. The information of the sound wave is coded on the optical spectrum of the sensor head by wavelength scanning, which builds a map between time and wavelength. The acoustic signal can be reconstructed from the sound-encoded spectrum. The sound-induced phase variation of the sensor can be interrogated by comparing the sound-encoded spectrum with the initial spectrum curve, which can be acquired from the sinusoidal fitting method. In order to eliminate the phase ambiguity, a diaphragm-based Michelson interferometer is set up using a commercial 3 $\times$ 3 fiber coupler and two synchronized channels with 120° phase difference are employed for the interrogation. Experimental results indicate that the proposed method can provide stable demodulation results under random environmental fluctuations, while the commonly used edge filtering technique shows fluctuations of more than 10 dB under the same condition.

Index Terms: Optical sensors, optical fiber devices, acoustic sensing, signal demodulation.

1. Introduction

Diaphragm-Based optical fiber acoustic sensors (OFAS) have been widely investigated due to its simple structure, compact size, and high sensitivity. Conventional types of OFAS include intensity-modulated sensors [1], [2], and phase-modulated structures such as Fabry-Perot interferometers (FPI) or Michelson interferometers (MI) formed by cleaved fiber end and diaphragm [3]–[12]. Compared with the intensity-modulated type, the interferometric phase-modulated structures have better performance in sensitivity and signal-to-noise ratio (SNR). The sound wave generates the vibration of the diaphragm, and thus the optical path difference (OPD) of the sensor is changed. Since the interferential phase is correlated with the OPD, the sound induced vibration of the diaphragm introduces phase modulation to the sensor, and the diaphragm deflection is proportional to the sound pressure [3]. Therefore the acoustic signal can be detected by demodulating the phase variation.

In order to recover the acoustic signal from the diaphragm-based OFAS, edge filtering technique is extensively used due to its simple operation [4]. By tuning the output wavelength of the laser source to the quadrature point (Q point), the acoustic pressure induced wavelength shift is converted to the optical intensity change. Obviously, this method requires complicated Q point tracking and stabilization techniques [5], [6], [13]. Without controlling the working point, the cavity length variation caused by the surrounding environmental fluctuations may cause signal fading [14]. Besides, the dynamic range of the edge filtering method is a dominant limiting factor in practical applications since the laser wavelength must locate in the linear range of the interferential spectrum, otherwise the output waveform will suffer from distortion. In order to overcome the shortcoming of dynamic range of edge filtering, phase demodulation based on different techniques have also been intensively studied, such as phase generated carrier (PGC) technology [15], [16] or two wavelength quadrature method [17], [18]. These methods have larger dynamic range than the edge filtering technique since the interrogated signal is optical phase of the interference spectrum so that it is not limited by the range of the linear region. However, these techniques usually require precise control of the external modulation signal (for PGC method) or single wavelength output in certain channels (for two wavelength method). Besides, the fluctuation of environmental factors such as temperature, pressure or humidity [19], [20] may also lead to phase variation (wavelength shift), which may degenerate the interrogation accuracy.

In this article, we proposed a novel phase interrogation method of diaphragm based optical fiber acoustic sensor with the assist of the wavelength-scanned spectral coding. The wavelength scanning builds a mapping relationship between the wavelength and time. Within this process, the time-varying acoustic information is coded on the sensor spectrum. The signal waveform can be reconstructed from the spectral coding function (SCF) by utilizing a phase interrogation algorithm. Since the slowly-varying environmental factors will introduce the same affect to both the spectra before and after coding procedure, the fluctuation of the interference caused by the random environmental factors can be eliminated in the interrogated signal by our proposed method. In experiment, we used a 3×3 fiber coupler to set up a Michelson interferometer (MI) as the sensor interferometer, and utilized two synchronized channels with 120° phase difference for interrogation to avoid phase ambiguity. Experimental results prove that our proposed method has a better performance in stability than edge filtering technique, which shows fluctuations of more than 10 dB under same environmental conditions.

2. Principle

2.1 Spectral Coding Mechanism

The spectral coding process is realized by the optical spectrum data acquisition method of wavelength scanning. In other words, the optical intensity at each wavelength is acquired at different time, therefore the wavelength scanning procedure builds a map between wavelength and time. In this way, the wavelength sampling is linearly related to time, while the acoustic sensor spectrum is time-varying caused by the dynamic sound pressure. As a consequence, the optical intensity at each wavelength sampling point records information of sound pressure at the corresponding time. The mechanism is demonstrated by Fig. 1 to make it more comprehensible.

In this figure, the red solid line is the initial interferential spectrum of the acoustic sensor in static condition (without sound wave applied), while the red dashed line simulates the sensor spectrum under a certain pressure (sound pressure at a certain time t_i). Imagine the optical intensity at a certain wavelength λ_n is sampled right at the moment t_i, the acquired intensity value will locate on the spectrum curve after sound pressure modulation (dashed line) rather than the initial curve (solid line), as depicted by the black dot in the figure. The deviation from the initial spectrum can be defined as the intensity coding amount. However, for phase-modulated type of acoustic sensor, the intensity variation results from the phase modulation, thus the phase variation value is in a linear relationship with the sound pressure, while the intensity modulation amount is not. Therefore, the phase modulation value is more suitable for the acoustic signal interrogation, as defined as the phase coding amount in the Fig. 1.

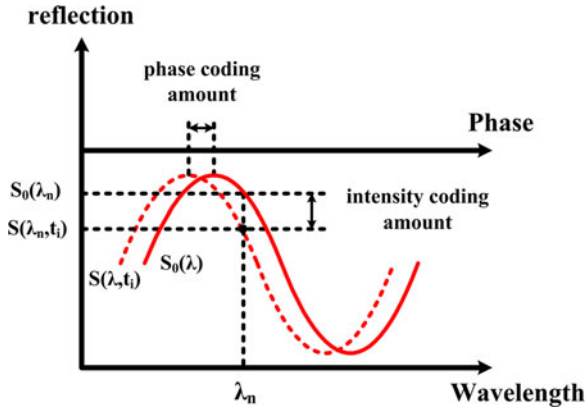

Fig. 1. Schematic diagram of the spectral coding mechanism.

For the sake of more accurate analysis, the theoretical explanation of the wavelength-scanned spectral coding mechanism is given below.

For diaphragm based interferometric fiber sensors such as low-finesse Fabry-Perot interferometers or Michelson interferometers, the reflected spectrum can be written as (1). In the applications of acoustic sensing, the time-varying optical path difference (OPD) will introduce a phase modulation item, so the optical spectrum will be a function of both wavelength and time, as demonstrated by (2) and (3). In (3), $\triangle L(t)$ is the OPD variation signal in time domain caused by the sound induced deflection of the diaphragm. The approximation in (3) indicates that the sound induced phase modulation can be regarded to be proportional to the OPD change. Therefore, this item can be selected to represent the acoustic signal as $a(t)$. According to the relationship between the wavelength and time connected by the scanning speed [21], the acoustic signal is coded onto wavelength domain, represented by a phase modulation item $x(\lambda)$, which is acquired from the shifting and stretching transformation of $a(t)$, as shown by (4). The starting wavelength λ_0 of the scanning range determines the shifting amount, while the wavelength scanning speed V (nm/s) represents the stretching scale factor. The encoded spectral function acquired by wavelength scanning is described by (4). Comparing (1) with (4), we can conclude that the acoustic signal is coded on the spectrum as a phase modulation item by the wavelength scanning procedure.

$$S_0(\lambda) = A + B\cos\left(\frac{4\pi L_0}{\lambda} + \varphi\right) \approx A + B\cos\left(\beta_0\lambda + \varphi\right) \tag{1}$$

$$S(\lambda, t) = A + B\cos\left[\beta_0\lambda + \varphi + \Delta\beta(t)\lambda\right] \tag{2}$$

$$\Delta\beta(t)\lambda = \frac{4\pi\Delta L\,(t)}{{\lambda_0}^2}\cdot\lambda \approx \frac{4\pi\Delta L\,(t)}{\lambda_0} = a(t) \tag{3}$$

$$S(\lambda) = A + B\cos\left[\beta_0\lambda + x(\lambda) + \varphi\right],\ x(\lambda) = a\left(\frac{\lambda - \lambda_0}{V}\right) \tag{4}$$

2.2 Phase Interrogation Algorithm

It is possible to reconstruct the acoustic signal by operations between the spectral coding function (SCF) $S(\lambda)$ and the static interferential spectrum (SIS) $S_0(\lambda)$. The SIS can be obtained by the sinusoidal fitting algorithm of the SCF. However, if only one channel of SCF data is adopted for the signal reconstruction, problem of phase ambiguity will occur, as demonstrated by the schematic diagram in Fig. 2.

Based on the diagram, the phase ambiguity can be explained as follows. When the spectrum is coded by the sound wave, the intensity at a wavelength may deviate from the SIS, as shown by the $S(\lambda_n)$ and $S_0(\lambda_n)$ in the figure. The SCF value at this wavelength should satisfy the interference

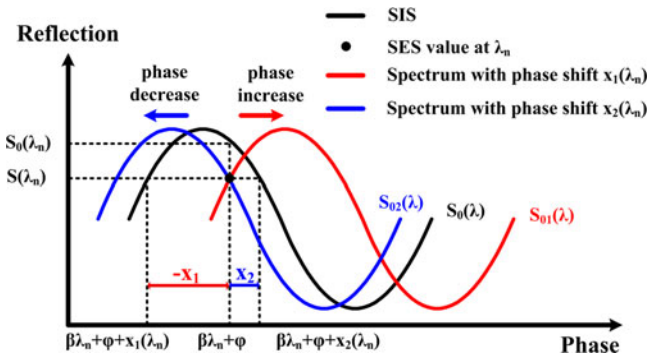

Fig. 2. Schematic diagram of phase ambiguity.

spectrum curve that has a certain phase shift with the SIS, as we have explained by Fig. 1 before. The phase shift is determined by the sound pressure at the time when the intensity at this wavelength is sampled. However, for a certain SCF value (black dot in Fig. 2) at its wavelength, there will be two possible conditions for the phase shift, as presented by the red and blue curves in Fig. 2. Here we only consider these two conditions since the sensitivity of diaphragm based acoustic sensors is usually lower than 160 nm/Pa [22], the dynamic range of the phase variation can be considered to be limited within the 2π region.

In order to avoid the phase ambiguity in the signal interrogation, we can utilize two channels with a certain phase difference $\triangle\varphi$ ($\triangle\varphi \neq m\pi$, m is an integer). The SIS and SCF of the two channels can be expressed by (5) and 6).

$$\begin{cases} S_{01}(\lambda) = A_1 + B_1 \cos[\beta_0\lambda + \varphi] \\ S_{02}(\lambda) = A_2 + B_2 \cos[\beta_0\lambda + \varphi + \Delta\varphi] \end{cases} \tag{5}$$

$$\begin{cases} S_1(\lambda) = A_1 + B_1 \cos[\beta_0\lambda + \varphi + x(\lambda)] \\ S_2(\lambda) = A_2 + B_2 \cos[\beta_0\lambda + \varphi + \Delta\varphi + x(\lambda)] \end{cases} \tag{6}$$

The parameters of the SIS function of the two channels can be sinusoidal fitted from the SCF data, including offset value (A_1 and A_2), contrast (B_1 and B_2), and phase difference $\triangle\varphi$. So the trigonometric part of the fitted SIS function can be obtained from these fitting data, expressed by the following (7).

$$T_{01}(\lambda) = \frac{S_{01}(\lambda) - A_1}{B_1}, \quad T_{02}(\lambda) = \frac{S_{02}(\lambda) - A_2}{B_2} \tag{7}$$

According to the above-mentioned SCF data and fitting parameters, we define three groups of intermediate parameters to realize the phase demodulation algorithm, as shown by the following (8).

$$\begin{cases} T_1(\lambda) = T_{01}(\lambda),\ T_2(\lambda) = \frac{T_{01}(\lambda)\cdot\cos\Delta\varphi - T_{02}(\lambda)}{\sin\Delta\varphi} \\ M_1(\lambda) = T_{02}(\lambda),\ M_2(\lambda) = T_1(\lambda)\cdot\sin\Delta\varphi + T_2(\lambda)\cdot\cos\Delta\varphi \\ N_1(\lambda) = \frac{S_1(\lambda) - A_1}{B_1},\ N_2(\lambda) = \frac{S_2(\lambda) - A_2}{B_2} \end{cases} \tag{8}$$

Based on these parameters, the sound induced phase variation $x(\lambda)$ can be computed from the following (9). The interrogated phase variation signal $x(\lambda)$ in the wavelength domain can be inversely transformed into the time domain to get the acoustic signal $a(t)$, as shown by (10).

$$x(\lambda) = tan^{-1}\left(\frac{N_1(\lambda)M_1(\lambda) - N_2(\lambda)T_1(\lambda)}{N_1(\lambda)M_2(\lambda) - N_2(\lambda)T_2(\lambda)}\right) \tag{9}$$

$$a(t) = x(\lambda_0 + Vt) \tag{10}$$

2.3 Discussion About the Detectable Frequency Limit

As we have discussed in the spectral coding mechanism, the scanning speed V builds a map between wavelength and time, and the sound signal is coded on the sensor spectrum. Owing to this principle, the detectable frequency range is determined by both the wavelength scanning speed V (nm/s) and the wavelength sampling interval $\triangle\lambda$ (nm), since the wavelength sampling interval determines the time-domain sampling interval of the interrogated signal through the map built by the scanning speed. The time-domain sampling frequency can be expressed by the following (11).

$$f_{smpl} = V/\Delta\lambda \tag{11}$$

According to the Nyquist sampling theory, the sampling frequency should be at least larger than twice as the signal frequency (sound frequency). In practical applications, the sampling frequency is usually set to be larger than five times of the sound frequency. Therefore, the upper limit of the detectable sound frequency can be explained by (12).

$$f_{\max} = V/5\Delta\lambda \tag{12}$$

Usually, the wavelength auto-scanned tunable laser source (TLS) or optical spectrum analyzer (OSA) can be adopted in our proposed interrogation scheme to function as the wavelength scanning device. So there should be one thing to notice that, for these kinds of devices, the wavelength scanning process works under a certain trigger frequency. In other words, the number of sampling points per second is set as a constant by the trigger series, so the wavelength scanning speed is determined by the wavelength sampling interval. This relationship can be demonstrated by the following (13), and the upper limit of the detectable sound frequency can be further derived.

$$V = f_{trigger} \cdot \Delta\lambda, \quad f_{\max} = f_{trigger}/5 \tag{13}$$

It can be seen that a higher upper frequency limit can be obtained by increasing the trigger frequency, which can be realized by setting a lower sampling sensitivity of the wavelength scanning device. However, the lower sensitivity will lead to the deterioration of the sensing accuracy. For this reason, there should be a trade-off between the upper frequency limit and the sensing accuracy. In our experimental demonstration, the scanning speed is 20 nm/s, while the sampling interval is 0.02 nm. The trigger frequency can be calculated to be 1000 Hz. According to the (13), the upper detectable frequency limit is 200 Hz, while the Nyquist limit is 500 Hz. Accordingly, the proposed method is mainly aiming at low-frequency acoustic sensing applications, for example, natural disaster forecast like earthquake and volcano eruption, health-structural monitoring, oil pipeline leakage detection, and even in military applications such as monitoring of nuclear explosion or rocket launching, etc.

3. Experimental Results and Discussion

3.1 Experimental Setup

In our experimental demonstration, we employed a commercial 3 $\times$ 3 fiber coupler to build two channels with 120° phase difference. The experimental setup is depicted in Fig. 3. A Michelson interferometer is formed by two arms of the 3 $\times$ 3 coupler. In the sensing arm, a piece of aluminum foil with 3 μm thickness is glued on the aperture of an ordinary flange plate by epoxy resin. Lead-in fiber is inserted into the flange plate to deliver light to the aluminum foil. The lead-in fiber has a tilted end face to avoid forming a FPI with the diaphragm though Fresnel reflection. In the reference arm, the fiber end face is cleaved to act as a reflector.

In the output ports, two optical spectrum analyzers (OSA, Yokogawa AQ 6370c) are employed to acquire the sensor spectra in two channels by wavelength scanning. The starting wavelength, stop wavelength, sensitivity and wavelength sampling interval of the two OSAs are set to be identical so that they have the same wavelength scanning speed and range. A signal generator produces synchronized square waves in two channels and inject them to the two OSAs to trigger the wavelength scanning process. The loudspeaker is driven by a function generator to produce

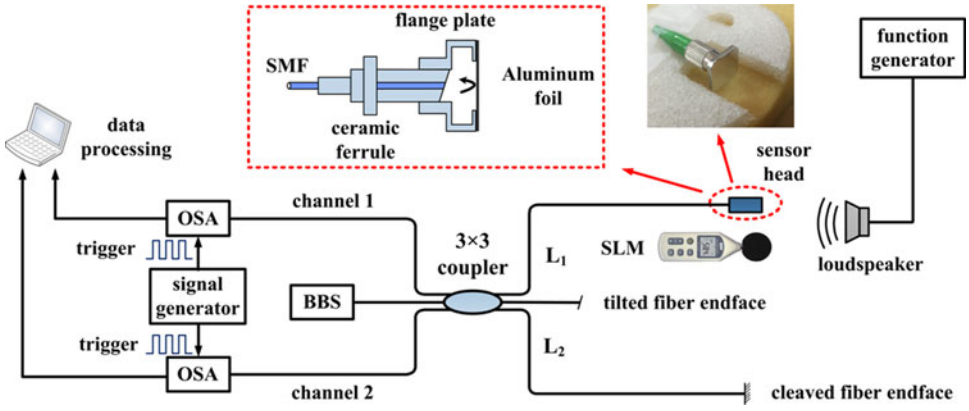

Fig. 3. Experimental setup to demonstrate the interrogation method.

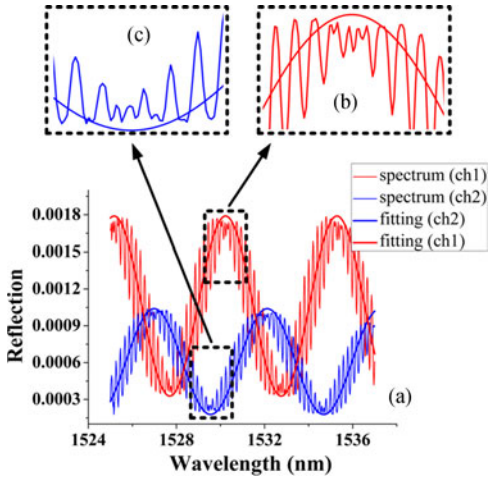

Fig. 4. Sound encoded spectrum of the proposed sensor under 100 Hz acoustic wave, (a) whole SCF curves and SIS fitted from SCF; (b) partial enlarged scale of the waveform distortion in channel 1 near the peak value; (c) partial enlarged scale of the waveform distortion in channel 2.

acoustic signal. A handheld sound level meter (SLM) is placed right beside the sensing head to calibrate the sound pressure. The distance from the loudspeaker to SLM is the same as that to the sensor head. In our experiment, this distance is set to be about 0.5 m. When the sound wave is applied to the sensor head, the two OSAs will record SCF data in the two channels. The sound induced phase modulation will be reconstructed from these data according to the aforementioned algorithm.

3.2 Validation Test

Our proposed phase interrogation scheme is experimentally validated by applying acoustic signal of 100 Hz sinusoidal waveform to the sensor head. The SCF curves of the two channels are plotted in Fig. 4(a). We can see the sinusoidal-analogous waveforms loaded on the interference spectra, and this phenomenon proves that the sound signal is coded on the spectrum in the wavelength domain, as predicted by the theoretical analysis. The SIS of the two channels are sinusoidal fitted respectively from the SCF data in each channel, as also plotted in Fig. 4. It is worth noting that the amplitude should be adjusted from the original fitting data. From (1) and (4) we can conclude that there should be no value in the SCF data that is larger than the maximum value of SIS, and

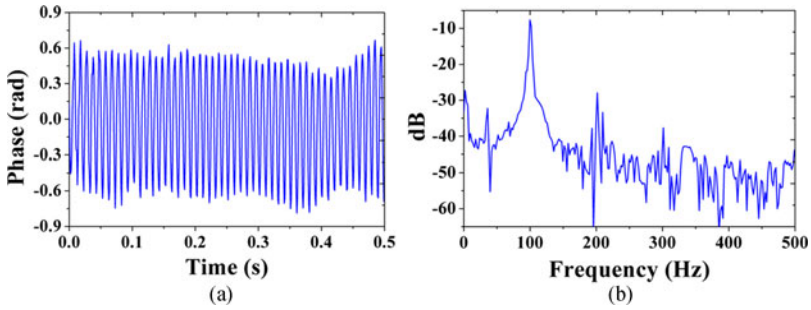

Fig. 5. Interrogated signal of the 100 Hz acoustic wave in (a) time domain; (b) frequency domain.

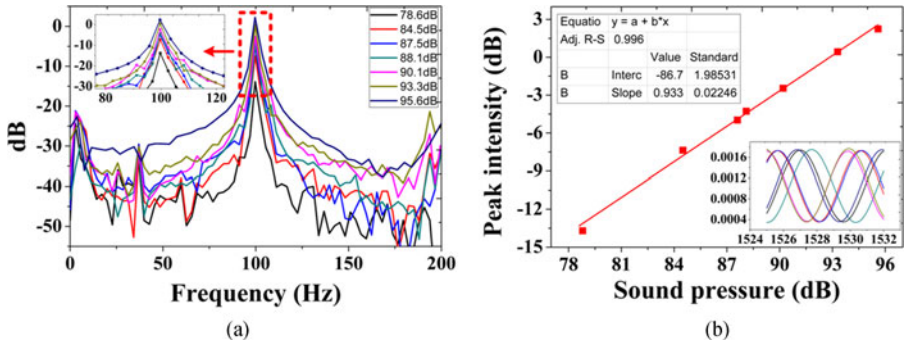

Fig. 6. (a) FFT spectra of the signals interrogated from the SCF data under different sound pressure; (b) relationship between the sound pressure and the dominant peak intensity.

also no SCF data smaller than the minimum value of SIS should exist. If not so, there might be no solution from the proposed algorithm at those points. Therefore the offset value and contrast of the SIS should be adjusted as the following (14).

$$\begin{cases} A' = \dfrac{\max(S(\lambda)) + \min(S(\lambda))}{2} \\ B' = \dfrac{\max(S(\lambda)) - \min(S(\lambda))}{2} \end{cases} \tag{14}$$

At the wavelength region that is close to the interference peaks or dips, the sinusoidal-analogous waveform will suffer from distortion, as can be seen from the partial-enlarged scales in Fig. 4(b) and (c). At these regions, the sound induced phase modulation (wavelength shift) will step over the interference peaks or dips, which leads to the distortion. The larger the sound pressure is, the wider the distortion regions will be. If only one channel of SCF data are used to reconstruct the signal, the distortion will affect the demodulated result within these regions due to the phase ambiguity. In our demonstration, we adopted the two reflected channels of the 3 $\times$ 3 coupler, and we can see an obvious phase difference between the two interferential spectra. The signal is interrogated through the proposed algorithm and plotted in Fig. 5(a) and (b).

3.3 Comparison to Edge Filtering Technique

In order to further evaluate the performance of the proposed interrogation method, we put forward an experiment to compare the results interrogated by the spectral coding method with frequently used edge filtering technique. Firstly we conducted a test by applying 100 Hz acoustic signal with sound pressure ranging from 78.6 dB to 95.6 dB to the sensor head, while the environmental factors are not controlled intentionally. The Fourier spectra of the interrogated signals under different sound pressure are plotted in Fig. 6(a). The dominant peak of the fast Fourier transform (FFT) spectrum

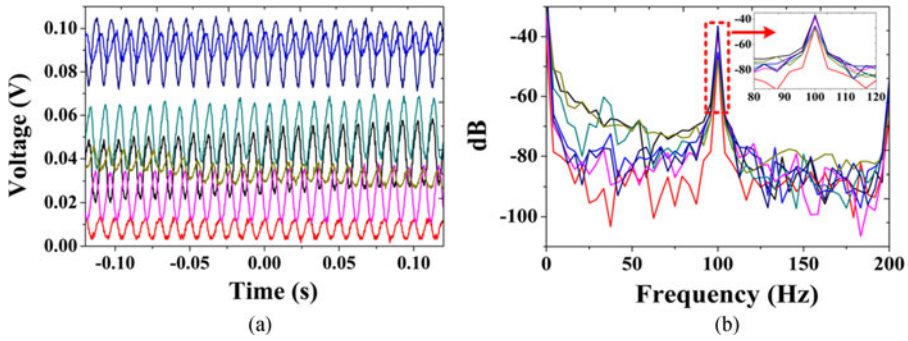

Fig. 7. (a) time domain signals and (b) FFT spectra of the edge filtering intensity demodulation results under the same laser power and acoustic signal.

at 100 Hz is partial enlarged and demonstrated in the inset. It can be seen from the inset that the dominant peak intensity is varying with the sound pressure. The relationship between the peak intensity and sound pressure in the logarithmic scale is linear fitted and plotted in Fig. 6(b). Good linearity with sensitivity approximate to 1 can observed, which means when the sound pressure increases 1 dB, it is the same for the peak intensity. The SIS of the channel 1 are obtained by sinusoidal fitting from the SCF curves under different sound pressure measured at different time, and the fitted SIS curves are plotted in the inset of Fig. 6(b). Obvious wavelength shift can be observed, which indicates the instability of the sensing head in the random environment situations. The wavelength shift is owing to the environmental factors fluctuation such as slow temperature drift of the aluminum foil and the two arms of the Michelson interferometer, etc. The good linearity of the sound pressure calibration using FFT peak intensity under random fluctuation of the sensing head shown in Fig. 6(b) states that the interrogated signals from the coded spectrum are isolated from the surrounding's instability. The detailed mechanism and analysis will be presented in the following section for discussion.

For comparison, we put forward the referenced experiment based on the commonly used edge filtering intensity demodulation method applying to the same sensing head. A 1570 nm laser source and a photodetector (PD) is adopted. The output power of the laser is fixed at 4.5 mW, while the sound pressure and frequency of the acoustic signal are kept stable at 84.5 dB and 100 Hz, respectively. We measured the intensity-demodulated signals several times under the same laser power and acoustic signal. The time domain waveforms and the corresponding FFT spectra are demonstrated in Fig. 7. It can be observed from Fig. 7(a) that the DC values and the amplitudes of the time-domain signals are all fluctuating under the fixed sound pressure. This is due to the Q point drift caused by the random wavelength shift that we have observed in the inset of Fig. 6(b). The dominant peak intensities in the FFT spectra in Fig. 7(b) are read out and plotted in Fig. 8. Under the same sound pressure, the peak intensities show fluctuations of more than 10 dB. The following analysis in the next section will explain that the peak intensity fluctuation is a symbol of the instability of the demodulation result, and it will have a serious impact on the sound pressure measurement when the sensor is in practical use.

3.4 Discussion

In this section, we firstly analyze the sound pressure calibration mechanism (relationship between the peak intensity of the FFT spectra and the sound pressure), and then we will discuss the experimental results based on the conclusion we have drawn. That is, the peak intensity (logarithmic scale) of the dominant frequency component is in a linear relationship with the sound pressure (logarithmic scale), and the linear coefficient is 1. To be more specifically, if the sound pressure increases (or decreases) by 1 dB, the peak intensity at the dominant frequency will also change by 1 dB. The theoretical analysis is given as follows.

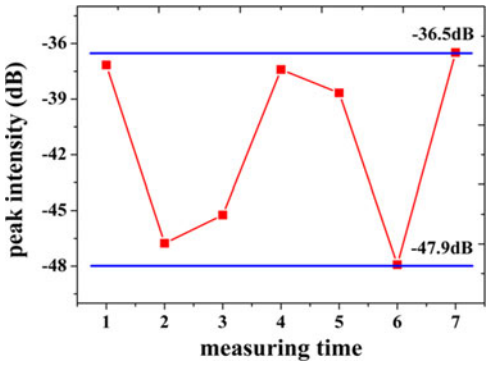

Fig. 8. Dominant peak intensity fluctuation of the FFT spectra under the same sound pressure.

For the phase modulation type of acoustic sensor, the phase variation should be proportional to the sound pressure, as expressed by the (15). In the equation, $a(t)$ is the time-domain acoustic signal that consists a series of frequency components ω_i, and P_i represents the sound pressure (Pascal) at each frequency. K is the phase sensitivity of the sensor to the sound pressure.

$$\varphi(t) = K \cdot a(t), a(t) = \sum P_i \cdot \cos(\omega_i t + \alpha_i) \tag{15}$$

In order to explain the relationship between the peak intensity at the dominant frequency and the sound pressure, we select one frequency for analysis, as shown in (16). φ_n stands for the interrogated time-domain phase variation signal that corresponds to the frequency component ω_n. The Fourier frequency spectrum of the interrogated result can be acquired from (17). Here the frequency spectrum is derived in the linear scale.

$$\varphi_n(t) = K \cdot P_n \cdot \cos(\omega_n t + \alpha_n) \tag{16}$$

$$F[\varphi_n(t)]_{lin} = K \cdot P_n \cdot F[\cos(\omega_n t + \alpha_n)] \tag{17}$$

If we define the intensity unit at the sound frequency component to be I_0 in the linear scale, as demonstrated by (18), we can express the peak intensity in the FFT spectrum using I_0, as (19). The peak intensity can be easily deduced from linear scale to logarithmic scale by (20).

$$F[\cos(\omega_n t + \alpha_n)]\big|_{\omega=\omega_n} = I_0 \tag{18}$$

$$I_{nlin} = F[\varphi_n(t)]_{lin}\big|_{\omega=\omega_n} = K \cdot P_n \cdot I_0 \tag{19}$$

$$I_{ndB} = 20\lg(K \cdot P_n \cdot I_0) \tag{20}$$

If the sound pressure at the frequency of ω_n varies from P_{n1} to P_{n2} (Pascal), the sound pressure variation in the logarithmic scale and the peak intensity of the frequency spectrum in the logarithmic scale can be respectively expressed by (21) and (22).

$$\Delta P_{ndB} = 20\lg\frac{P_{n2}}{20\mu Pa} - 20\lg\frac{P_{n1}}{20\mu Pa} = 20\lg\frac{P_{n2}}{P_{n1}} \tag{21}$$

$$\Delta I_{ndB} = 20\lg(K P_{n2} I_0) - 20\lg(K P_{n1} I_0) = 20lg\frac{P_{n2}}{P_{n1}} \tag{22}$$

From these two equations we can find that the peak intensity change equals to the sound pressure variation in the logarithmic scale. This conclusion proves that the peak intensity in the FFT spectrum can be adopted to calibrate the sound pressure.

Based on this conclusion, the peak intensity fluctuation of the edge filtering results shown in Figs. 7 and 8 indicate that the calibrated sound pressure will have an uncertainty of at least 10 dB in practical use. The peak intensity fluctuation comes from the amplitude fading of the time-domain

signals demonstrated in Fig. 7(a), which results from the Q point drift in the random environment. The amplitude fading changes the phase sensitivity K (defined in (15)) to the sound pressure, and thus leading to different FFT peak intensity values under the same sound pressure.

Compared to the edge filtering results, the interrogated signals by our proposed spectral coding method perform well under the fluctuation of the sensing head, as shown by Fig. 6. This property can be explained by the following (23), in which φ_e represents the phase fluctuation introduced by the environmental factors' instability. It can be seen that the SIS and SCF experience the same phase fluctuation, and it can be eliminated by the fitting and differential process in the phase interrogation algorithm mentioned above.

$$\begin{cases} S_0(\lambda) = A + B\cos\left[\beta_0\lambda + x(\lambda) + \varphi + \varphi_e\right] \\ S(\lambda) = A + B\cos\left[\beta_0\lambda + x(\lambda) + \varphi + \varphi_e\right] \end{cases} \tag{23}$$

According to the sound pressure calibration mechanism and the performance comparison of the two interrogation methods using the same sensing head, the evidence of stability of the spectral coding method is enhanced.

4. Conclusion

To summarize, we proposed a novel interrogation method for the diaphragm based fiber acoustic sensor by reconstructing the phase variation from the spectral coding procedure. The acoustic information can be coded on the sensor spectrum by wavelength scanning process and experiences conversion from time domain to wavelength domain. The inter-domain coding procedure and the proposed phase interrogation algorithm can eliminate the phase fluctuation of the sensor introduced by the environmental instability, which is both theoretically analyzed and experimentally demonstrated.

References

[1] M. NessAiver, M. Stone, V. Parthasarathy, Y. Kahana, and A. Paritsky, "Recording high quality speech during tagged cine-MRI studies using a fiber optic microphone," *J. Magn. Reson.*, vol. 23, no. 1, pp. 92–97, Jan. 2006.

[2] S. Wang, P. Lu, L. Zhang, D. Liu, and J. Zhang, "Optical fiber acoustic sensor based on nonstandard fused coupler and aluminum foil," *IEEE Sensors J.*, vol. 14, no. 7, pp. 2293–2298, Jul. 2014.

[3] J. Ma, H. Xuan, H. Ho, W. Jin, Y. Yang, and S. Fan, "Fiber-optic Fabry–Perot acoustic sensor with multilayer graphene diaphragm," *IEEE Photon. Technol. Lett.*, vol. 25, no. 10, pp. 932–935, May 2013.

[4] S. Wang *et al.*, "An infrasound sensor based on extrinsic fiber-optic Fabry–Perot interferometer structure," *IEEE Photon. Technol. Lett.*, vol. 28, no. 11, pp. 1264–1267, Jun. 2016.

[5] F. Wang, Z. Shao, J. Xie, Z. Hu, H. Luo, and Y. Hu, "Extrinsic Fabry–Pérot underwater acoustic sensor based on micromachined center-embossed diaphragm," *J. Lightw. Technol.*, vol. 32, no. 23, pp. 4026–4034, Dec. 2014.

[6] Z. Gong *et al.*, "High-sensitivity fabry-perot interferometric acoustic sensor for low-frequency acoustic pressure detections," *J. Lightw. Technol.*, vol. 35, no. 24, pp. 5276–5279, Dec. 2017.

[7] Y. Wu *et al.*, "A highly sensitive fiber-optic microphone based on graphene oxide membrane," *J. Lightw. Technol.*, vol. 35, no. 19, pp. 4344–4349, Oct. 2017.

[8] W. Zhang *et al.*, "An optical fiber Fabry-Pérot interferometric sensor based on functionalized diaphragm for ultrasound detection and imaging," *IEEE Photon. J.*, vol. 9, no. 3, May 2017, Art. no. 7103208.

[9] Q. Rong *et al.*, "Ultrasonic sensitivity-improved Fabry–Perot interferometer using acoustic focusing and its application for noncontact imaging," *IEEE Photon. J.*, vol. 9, no. 3, May 2017, Art. no. 6802511.

[10] C. Jan, W. Jo, M. J. F. Digonnet, and O. Solgaard, "Photonic-crystal-based fiber hydrophone with sub-100 μPa/$\sqrt{}$Hz pressure resolution," *IEEE Photon. Technol. Lett.*, vol. 28, no. 2, pp. 123–126, Jan. 2016.

[11] L. Liu *et al.*, "UV adhesive diaphragm-based FPI sensor for very-low-frequency acoustic sensing," *IEEE Photon. J.*, vol. 8, no. 1, Feb. 2016, Art. no. 6800709.

[12] L. Liu *et al.*, "Fiber-optic michelson interferometric acoustic sensor based on a PP/PET diaphragm," *IEEE Sensors J.*, vol. 16, no. 9, pp. 3054–3058, May 2016.

[13] J. Ma, M. Zhao, X. Huang, H. Bae, Y. Chen, and M. Yu, "Low cost, high performance white-light fiber-optic hydrophone system with a trackable working point," *Opt. Exp.*, vol. 24, no. 17, pp. 19008–19019, Aug. 2016.

[14] J. Chen, W. Li, H. Jiang, and Z. Li, "Stabilization of a fiber Fabry–Perot interferometric acoustic wave sensor," *Microw. Opt. Technol. Lett.*, vol. 54, no. 7, pp. 1668–1671, Aug. 2012.

[15] F. Wang, J. Xie, Z. Hu, S. Xiong, H. Luo, and Y. Hu, "Interrogation of extrinsic Fabry–Perot sensors using path-matched differential interferometry and phase generated carrier technique," *J. Lightw. Technol.*, vol. 33, no. 12, pp. 2392–2397, Jun. 2015.

[16] B. Liu, J. Lin, H. Liu, Y. Ma, L. Yan, and P. Jin, "Diaphragm based long cavity Fabry–Perot fiber acoustic sensor using phase generated carrier," *Opt. Commun.*, vol. 382, pp. 514–518, 2017.
[17] H. Liao *et al.*, "Phase demodulation of short-cavity Fabry–Perot interferometric acoustic sensors with two wavelengths," *IEEE Photon. J.*, vol. 9, no. 2, Apr. 2017, Art. no. 7102207.
[18] J. Xia, S. Xiong, F. Wang, and H. Luo, "Wavelength-switched phase interrogator for extrinsic Fabry–Perot interferometric sensors," *Opt. Lett.*, vol. 41, no. 13, pp. 3082–3085, Jul. 2016.
[19] M. Llera *et al.*, "Liquid-air based Fabry–Pérot cavity on fiber tip sensor," *Opt. Exp.*, vol. 24, no. 8, pp. 8054–8065, Apr. 2016.
[20] M. Yang *et al.*, "Dielectric multilayer-based fiber optic sensor enabling simultaneous measurement of humidity and temperature," *Opt. Exp.*, vol. 22, no. 10, pp. 11892–11899, May 2014.
[21] X. Fu et al., "Spectrum interrogation of fiber acoustic sensor based on self-fitting and differential method," *Opt. Exp.*, vol. 25, no. 4, pp. 4429–4437, Feb. 2017.
[22] F. Xu, J. Shi, K. Gong, H. Li, R. Hui, and B. Yu, "Fiber-optic acoustic pressure sensor based on large-area nanolayer silver diaghragm," *Opt. Lett.*, vol. 39, no. 10, pp. 2838–2840, May 2014.